steel research international

A Water Experiment Benchmark to Evaluate Numerical Models for the Motion of Particles in Continuous Casting Tundish

Alexander Vakhrushev,* Menghuai Wu, Andreas Ludwig, Gerald Nitzl, Yong Tang, Gernot Hackl, and Raimund Wincor

This paper presents a water experiment benchmark for evaluation of the numerical models for the particle motion in a continuous casting tundish. The particles are optically tracked in the model tundish and additionally are captured by instrumented wooden frames at the water surface. In the meantime, an attempt is made to simulate the water flow and motion of the particles by using the Eulerian–Lagrangian approach. It is shown that for the experiment with large particles (ϕ3.5 mm) the experimentally determined distribution of the particles as captured by the wooden frames can be numerically simulated, but for the small particles (with a diameter distribution between 50 and 600 μm) there is still relative large mismatch between the simulation and the experiment. Some modeling options and parameters must be tuned carefully. This raises concern for the future application of the models in real engineering process where experimental calibration and evaluation are not possible. Therefore, the goal of this paper is to (i) call contributions from researchers to propose their models and evaluate them against the same benchmark; (ii) verify the agreement of the numerical solutions obtained by different contributors, and (iii) comment on further improvements and modifications to the existing models.

1. Introduction

Understanding the transport behavior of the non-metallic inclusions (particles) in molten steel is an important topic in the primary and secondary metallurgy.[1,2] For example, reduction of the non-metallic inclusions (NMIs) by stirring the ladle,[3] removal of the NMIs in the tundish of the continuous caster by controlling the flow,[4] flotation of the NMIs in continuous casting mold so as to minimize the risk of capturing those inclusions into the solidified steel product[2] are of great interest for metallurgists. Because it is extremely difficult to investigate above phenomena experimentally at the laboratory or at the plant during the casting operation, the numerical modeling approaches become in favor. Therefore, diverse models were proposed. The most popular model is based on Eulerian–Lagrangian approach, i.e., the transient flow of the melt is calculated by solving Navier–Stokes equation in the Eulerian framework, while the motion of particles is tracked in the Lagrangian framework. For example, Thomas et al.[5] and the current authors[6] used this method to calculate the motion of NMIs in continuous caster, and to predict the entrapment of NMIs by the solidifying shell. Some people used a two-phase Eulerian–Eulerian approach to model this problem, i.e., cloud of particles is treated as a continuum phase (a secondary fluid phase) which interacts with the melt (the primary fluid phase). For example, Javurek et al. used this method to calculate the transport of NMIs by the melt flow in a steel strand, where the gravity-induced relative motion between the NMIs and the primary phase (melt) is modeled as the so-called drift velocity.[7] Some other numerical methods, such as the Lattice-Boltzmann[8] and the discrete element method (DEM), [9] were also under development for the issue of the particle motions, and they might find more applications in the field of metallurgy in future.

[*] Dr. A. Vakhrushev, Prof. M. Wu
Christian Doppler Laboratory for Advanced Process Simulation of Solidification and Melting, Department of Metallurgy, Montanuniversitaet Leoben, Franz-Josef-Str. 18, 8700, Leoben, Austria
Email: alexander.vakhrushev@unileoben.ac.at
Prof. M. Wu, Prof. A. Ludwig
Chair of Simulation and Modeling of Metallurgical Processes, Department of Metallurgy, Montanuniversitaet Leoben, Franz-Josef-Str. 18, 8700, Leoben, Austria
G. Nitzl
RHI AG, Wienerbergstrasse 9, 1100 Vienna, Austria
Dr. Y. Tang, G. Hackl
RHI AG, Technology Center, Magnesitstrasse 2, 8700 Leoben, Austria
R. Wincor
voestalpine Stahl GmbH, VOEST-ALPINE Strasse 3, P.O. Box 3, 4031, Linz, Austria

DOI: 10.1002/srin.201600276

The major drawback to perform numerical modeling of this issue is that a lot of modeling options and modeling parameters are to be determined or arbitrarily chosen, no matter which of the above numerical approaches is used. Experimental data available to validate the numerical models are very limited. Rückert et al. presented a particle–water experiment based on a 1-to-3 continuous casting tundish model, providing data for the particle distribution at the symmetry plane and the particle separation rate based on the flow Reynolds number and the tundish geometry.[10] A good match between the numerical simulation and the experiment was achieved after introducing a special separation condition in the commercial software FLUENT, but still a slight divergence of the results was observed.

In the current paper, the authors present a benchmark of water experiment based on the 1-to-1 model of a continuous casting tundish by injecting plastic particles through the inflow into the tundish to mimic the transport behavior of NMIs in the molten steel. Particles, which are floated to the water surface of the tundish, are captured by means of a special wooden frame being mounted on the top of the tundish water model. The final integral distribution of the particles at the top surface provides valuable information for evaluation of numerical models.

The goal of this work is to call contributions from other researchers, and to evaluate their models based on the same settings of the benchmark; to verify the agreement of the numerical solutions by different contributors. Odenthal et al. have published a water model benchmark for an under-scaled industry tundish with well-documented flow measurement.[11] The current paper, however, focuses on the motion of particles.

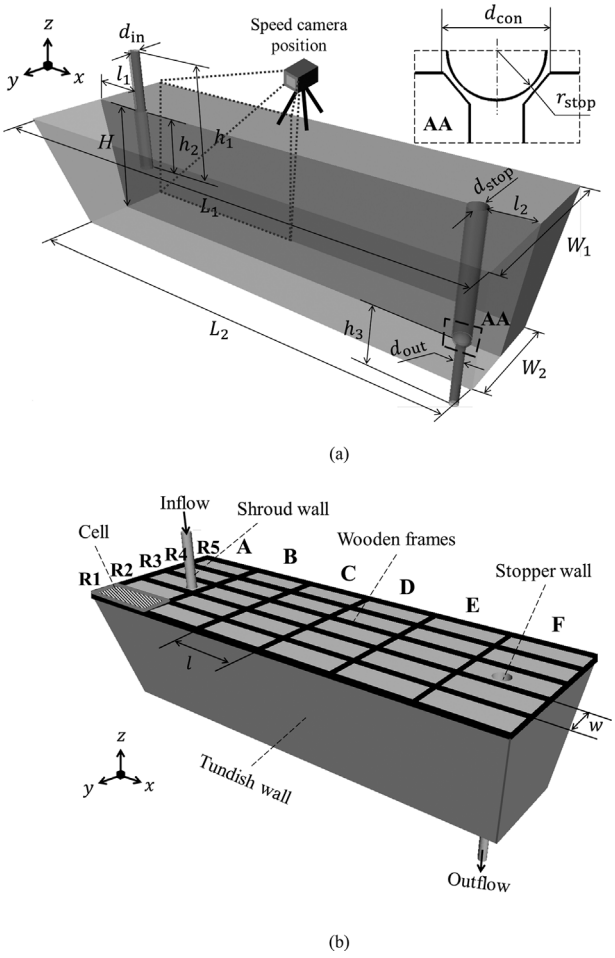

Figure 1. Experimental setup: a) tundish dimensions; b) layout of the wooden frame.

2. Water Modeling Experiment

The water model facility includes 1-to-1 Plexiglas model of a full-scale industry continuous casting tundish (**Figure 1**). The dimensions of the experiment setup are summarized in **Table 1**. The transparency of the tundish wall allows recording the motion of particles with a high-speed camera. The water experiment includes inflow and outflow, which connect with each other as a loop. A water pump is employed to provide a steady water flow with a controlled volume flow rate (0.426 $m^3\,min^{-1}$). Two types of particles (called hereinafter large and small) are prepared for two different experiments. The producers of particles are: Borealis Polyolefine GmbH (Linz, Austria) for the large particles (diameter of ϕ3.5 mm) and Licowax Clariant GmbH (Frankfurt am Main, Germany) for the small particles with a diameter distribution between 50 and 600 μm. Properties of particles and some injection parameters are listed in **Table 2**. Shape of particles is spherical for both types, and the diameter for the large ones is considered uniform. The size distribution of the small particles is given in **Table 3**. A high-speed video camera is implemented to record the particle distribution in the tundish (Figure 1). Additionally, an immersed wooden frame (≈20 mm in wall thickness, immersion depth of 50 mm) is mounted on the top of the tundish to capture the floating particles. At the end of experiment, the particles as captured by each cell of wooden frame are dried and their mass is weighted. A slight transversal motion of the particles from one cell to its neighboring cells is observed during experiment, but it has only ignorable influence on the final result of the measurement.

The water flow experiment starts before injection of any particle. It lasts approximately 10 min until a quasi-steady state flow pattern in the tundish is established. Then injection of the particles through the shroud starts. As shown in Table 2, two experiments are made: one for large particles (diameter of 3.5 mm) and one for small particles. As soon as particles are injected, the video camera starts to record the particle distributions in the shroud pipe and in the tundish. The durations of particle injection for two experiments are also different (see Table 2). After the particle injection the experiment continues until all

Dimensions	Size [mm]	Dimensions	Size [mm]
L_1, top length	3975.3	l_2, stopper position	320.0
L_2, bottom length	3685.0	d_{stop}, stopper diameter	136.0
W_1, top width	1351.9	d_{con}, connector diameter	140.0
W_2, bottom width	766.0	h_1, shroud height	1020.0
H, tundish height	1000.0	h_2, shroud immersion depth	520.0
d_{in}, inlet diameter	90.0	h_3, outlet height	550.0
d_{out}, outlet diameter	69.3	l, frame cell length	662.5
l_1, shroud position	485.0	w, frame cell width	270.4

Table 1. Tundish dimensions. Symbols are marked in Figure 1.

Experiment number	Diameter of particles [mm]	Density of particles [kg m^{-3}]	Mass injection rate of particles [kg s^{-1}]	Total particle injection time [s]	Average water flow rate [m^3 min^{-1}]
Exp. 1	3.5	950.0	0.0581	32.0	0.426
Exp. 2	distribution (see Table 3)	920–940	0.0581	16.0	0.426

Table 2. Particle densities and injection parameters.

particles in the tundish disappear. It means that all particles float to the top water surface and captured by the wooden frame, or some of them escape through the outflow.

The experimental results include the video sequence of the particle distribution, **Figure 2**, corresponding to different moments, and the weighted particles as captured by wooden frame in each cell, as summarized in **Table 4** and **5**. As supplementary materials, the video records of the entire water experiment are available by contacting the authors.

3. Numerical Simulation

An Eulerian–Lagrangian model, as implemented by the authors[12] in an open-source CFD package OpenFOAM,[13] is applied to calculate the above benchmark. As the particle injection mass flow rate is 0.82 wt% (corresponding to 0.86–0.88 vol%) compared to the continuous phase (see Table 2), the Discreet Particle Method is valid and can be applied. The flow of the water is calculated by solving Navier–Stokes equation in the Eulerian framework. The continuous medium (water) represents an incompressible fluid with variable viscosity dependent on the local turbulent kinetic energy and its dissipation rate. The Finite Volume Method (FVM) is used with a so-called collocated or non-staggered variable arrangement,[14,15] where all transport quantities share the same control volumes (CV), and all flux variables reside on the CV faces.

3.1. General Equations

The basic equations of the Eulerian approach for the water flow are (1) continuity and (2) momentum conservation

wt%	ϕ [μm]	wt%	ϕ [μm]	wt%	ϕ [μm]	wt%	ϕ [μm]	wt%	ϕ [μm]
5	< 56.9	25	< 162.78	45	< 240.79	65	< 318.68	85	< 425.17
10	< 91.4	30	< 183.35	50	< 259.42	70	< 340.89	90	< 463.86
15	< 117.7	35	< 203.08	55	< 278.33	75	< 365.73	95	< 508.65
20	< 141.0	40	< 222.21	60	< 297.85	80	< 393.6	100	< 564.21

Table 3. Distribution of the diameter classes for the small particles.

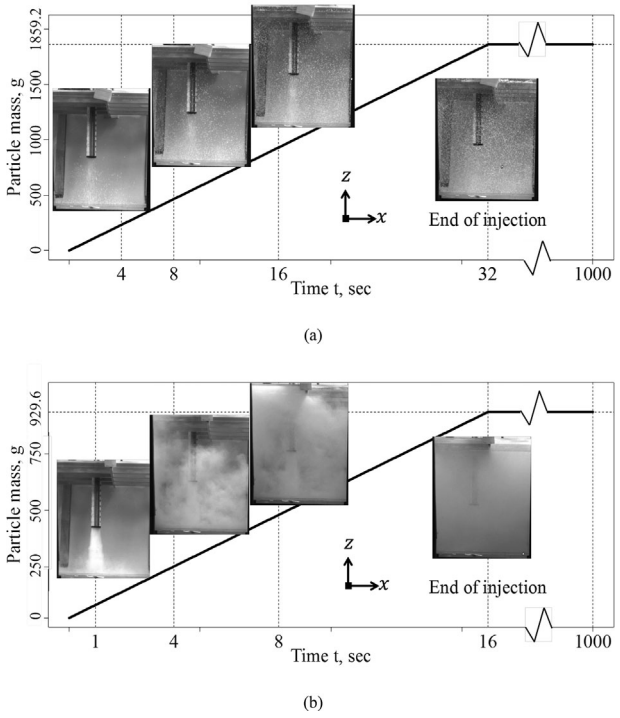

Figure 2. Injection history: a) experiment 1 for particles of diameter 3.5 mm; b) experiment 2 for particles of diameter distribution between 50 and 600 μm. The solid curves show the total mass of particles injected through the shroud into the tundish. Particle distributions in the tundish at some moments, as recorded by speed camera, are shown.

equations:

$$\nabla \cdot \mathbf{u} = 0 \tag{1}$$

$$\rho \frac{\partial \mathbf{u}}{\partial t} + \rho \nabla \cdot (\mathbf{u} \otimes \mathbf{u}) = \nabla (2\mu_{\text{eff}} \text{dev}(\dot{\boldsymbol{\varepsilon}})) - \nabla p \tag{2}$$

defining the effective dynamic viscosity as a sum of the molecular and the turbulent ones $\mu_{\text{eff}} = \mu_\ell + \mu_\text{t}$; the rate-of-strain tensor is a symmetric part of the velocity gradient tensor:

$$\dot{\boldsymbol{\varepsilon}} = \text{Sym}(\nabla \mathbf{u}) = \frac{1}{2}\left(\nabla \mathbf{u} + (\nabla \mathbf{u})^T\right) \tag{3}$$

For the closure of the model equation system (1)–(3) a RANS approach, based on k–ε model,[16,17] is used to model the turbulence. Here the standard k–ε model is employed with the following transport equations for the turbulence kinetic energy and its dissipation rate[18]

$$\frac{\partial(\rho k)}{\partial t} + \nabla \cdot (\rho \mathbf{u} k) = \nabla \cdot \left(\left(\mu_\ell + \frac{\mu_\text{t}}{\text{Pr}_{\text{t,k}}}\right)\nabla k\right) + G - \rho\varepsilon \tag{4}$$

$$\frac{\partial(\rho \varepsilon)}{\partial t} + \nabla \cdot (\rho \mathbf{u} \varepsilon) = \nabla \cdot \left(\left(\mu_\ell + \frac{\mu_\text{t}}{\text{Pr}_{\text{t},\varepsilon}}\right)\nabla \varepsilon\right) + C_{1\varepsilon} G \frac{\varepsilon}{k} - \rho C_{2\varepsilon} \frac{\varepsilon^2}{k} \tag{5}$$

where the turbulent viscosity and the production term for the turbulent kinetic energy are

$$\mu_\text{t} = \rho C_\mu \frac{k^2}{\varepsilon} \tag{6}$$

$$G = 2\mu_\text{t} \|\dot{\boldsymbol{\varepsilon}}\|^2 \tag{7}$$

On the one hand, the standard k–ε model is known for the higher numerical diffusivity if compared to other RANS-family models. On the other hand, it allows achieving a quasi-steady state flow more easily, especially by using a first order discretization. It should be noticed that for the higher order of discretization the predicted flow becomes more transient and asymmetric, which makes the verification of the numerical solutions by different models more difficult.

Mass [g]	A	B	C
R1	118.81	58.95	12.72
R2	305.03	192.03	28.27
R3	335.29	122.01	7.79
R4	295.74	171.55	28.94
R5	127.34	43.32	12.11

Table 4. Weighted particles as captured by wooden frame in each cell; experiment 1 for the particle diameter of 3.5 mm; total mass of particles captured by the wooden frame: 1859.9 g; no particle escaped from the outflow.

Mass [g]	A	B	C	D
R1	43.98	35.76	7.85	9.25
R2	85.1	62.67	30.27	11.68
R3	74.68	46.35	19.24	13.33
R4	78.85	52.57	25.79	9.37
R5	29.5	55.68	1.46	5.5

Table 5. Weighted particles as captured by wooden frame in each cell; experiment 2 for the particle diameter distribution (50–600 μm); total mass of particles captured by the wooden frame: 698.9 g; total mass of particles escaped from outflow: 230.7 g (estimated).

The motion of particles is tracked within the Lagrangian framework. Each particle is provided with its own position vector $\mathbf{x}_P$ in the Cartesian system of coordinates. To determine the particle's velocity $\mathbf{u}_P$ and its acceleration, $d\mathbf{u}_P/dt$, it is sufficient to compute the time derivatives of the trajectory vector $\mathbf{x}_P$ of the corresponding order. A number of forces are taken into account, namely drag, buoyance, virtual mass, lift and pressure gradient forces:

$$m_P \frac{d\mathbf{u}_P}{dt} = \mathbf{F}_D + \mathbf{F}_B + \mathbf{F}_V + \mathbf{F}_L + \mathbf{F}_P \tag{8}$$

where the particle mass and the particle velocity are calculated as follows:

$$m_P = \rho_P \frac{1}{6} \pi D_P^3 \tag{9}$$

$$\frac{d\mathbf{u}_P}{dt} = \frac{d^2\mathbf{x}_P}{dt^2} \tag{10}$$

A particle drag force, based on the relative velocity $\mathbf{u} - \mathbf{u}_P$ between the continuous and discreet phase for a spherical particle is defined by the relation

$$\mathbf{F}_D = \frac{1}{8} \pi \rho D_P^2 C_D |\mathbf{u} - \mathbf{u}_P| (\mathbf{u} - \mathbf{u}_P) \tag{11}$$

The Schiller–Naumann approximation is used for the drag coefficient:[19]

$$C_D = \begin{cases} \dfrac{24}{Re_P}, & \text{if } Re_P \le 0.1; \\ \dfrac{24}{Re_P}\left(1 + 0.15 Re_P^{0.687}\right), & \text{if } 0.1 \le Re_P \le 10^3; \\ 0.44, & \text{if } Re_P > 10^3. \end{cases} \tag{12}$$

where the particle Reynolds number is

$$Re_P = \frac{\rho D_P |\mathbf{u} - \mathbf{u}_P|}{\mu_\ell} \tag{13}$$

Buoyancy force acting on a particle in a liquid flow can be calculated

$$\mathbf{F}_B = \frac{1}{6} \pi D_P^3 (\rho_P - \rho) \mathbf{g} \tag{14}$$

Virtual (added) mass force for the particles is estimated according to the next relation:[20]

$$\mathbf{F}_V = \frac{\rho \pi D_P^3}{12} \left(\frac{D\mathbf{u}}{Dt} - \frac{d\mathbf{u}_P}{dt} \right) \tag{15}$$

For the Saffman's lift force the following equation based on the particle shear Reynolds number Re_G is applied:[21,22]

$$\mathbf{F}_L = \frac{9}{\pi} \frac{D_P}{2} \mu (\mathbf{u} - \mathbf{u}_P) \sqrt{Re_G}\ \mathrm{sgn}(\dot{\gamma}) \tag{16}$$

$$Re_G = \frac{\rho D_P^2}{\mu} |\dot{\gamma}| \tag{17}$$

Finally, the pressure gradient force is included in the particle force balance (8):

$$\mathbf{F}_P = -\frac{\pi D_P^3}{6} \rho u_{p_i} \frac{\partial u_i}{\partial x_i} \tag{18}$$

The complexity of the particle interaction with turbulent eddies of the viscous flow is taken into account with a Discrete Random Walk model.[23,24] For simplicity a one-way coupling between the water flow and the particle motion is considered: the water flow influences the motion of particles; while the influence of the motion of particles on the water flow is ignored.

According to Graham and James,[23,24] a turbulent eddy affects a single spherical particle trajectory during a specific time t_P^{DRW}, which can be estimated based on several eddy time and length scales for the local turbulence parameters:

$$t_{eddy} = -0.15 \frac{k}{\varepsilon} \log r \tag{19}$$

$$t_{cross} = -\tau_P \ln \left[1 - \left(\frac{L_{eddy}}{\tau_P |\mathbf{u} - \mathbf{u}_P|} \right) \right] \tag{20}$$

$$L_{eddy} = \sqrt{C_\mu} \frac{k^{3/2}}{\varepsilon} \tag{21}$$

$$\tau_P = \frac{4}{3} \frac{\rho_P D_P}{\rho C_D |\mathbf{u} - \mathbf{u}_P|} \tag{22}$$

$$t_P^{DRW} = \min\left\{ t_{eddy}, t_{cross} \right\}. \tag{23}$$

During the eddy-particle interaction time an additional stochastic velocity component is applied:

$$\mathbf{u}' = \boldsymbol{\zeta} \sqrt{\frac{2k}{3}} \tag{24}$$

leading to the modified form of the drag force (11):

$$\mathbf{F}_D = \frac{1}{8}\pi \rho D_P^2 C_D |\mathbf{u} - \mathbf{u}_P|(\mathbf{u} + \mathbf{u}' - \mathbf{u}_P) \quad (25)$$

Particle–wall interaction mechanism is considered by introducing wall friction and restitution coefficients, decreasing the normal and tangential components of the particle velocity according to

$$\tilde{\mathbf{u}}_P = -\varepsilon_{wall}\mathbf{u}_P^{\mathbf{n}} + (1 - \mu_{wall})\mathbf{u}_P^{\boldsymbol{\tau}} \quad (26)$$

3.2. Numerical Model Settings

The following settings for flow calculation were made: the calculation domain consists of 1.96 million CVs and the mesh file is available by contacting the authors; the calculation time step is 0.001 s. One flow calculation for a physical time of 1000 s takes ≈13 days on a high performance cluster (2.6 GHz, 12 cores). Settings for tracking particles: the total number of particles for experiment 1 with the particle diameter of 3.5 mm is 0.1 million; the total number of particles for experiment 2 with particle diameter distribution is 0.65 million; the calculation time step is 0.005 s. One calculation for particle tracking takes ≈33 h for experiment 1 with large particles and ≈8 days for experiment 2 with small particles on a high performance cluster (2.6 GHz, 12 cores). It should be noticed that it is not possible to calculate all number of particles for the experiment 2, because there are too many particles (0.65 billion). Therefore, the total number of particles for experiment 2 is reduced by a factor of 0.001. The computational efficiency of the simulation was improved by reducing the diameter classes of particles to 10 groups (see **Table 6**), instead of the 20 groups (see Table 3). Other model settings including physical properties are listed in **Table 7**. All boundary conditions are summarized in Table 7. A bouncing model (26) is implemented to treat the particle–wall interaction. To record the distribution of particles as captured by the wooden frame, a top surface boundary is divided into 30 patches with the area, corresponding to the cells of the wooden frame (Figure 1b). As a particle reaches the top boundary, belonging to a special patch, it is removed from the domain and it is recorded as a captured particle by this patch. Particles escaping from the outflow are also removed and recorded.

3.3. Initialization of the Flow Field

The calculated flow in the tundish is transient and in 3D nature. **Figure 3** shows the flow field at a moment after 1000 s (physical time). Even though a standard k–ε model is used, the calculated velocity field is still unstable. The velocity vectors in five vertical sections (A–E) show that the flow is not symmetric, and it indicates that some large vortices develop in the tundish. This global flow pattern is actually quite similar to that as published by Odenthal et al.[11] for an under-scaled tundish water model. One confirmed feature of the flow in this kind of tundish with a single port of outflow is that a backward flow is predicted in the middle region between the shroud and the stopper rod, as seen in the symmetry plane (Figure 3a). This backward flow leads to formation of a vortex in the position near the C section. The x-component of the velocity along the line F–F, which lies on the symmetry plane and crosses the vortex center, is plotted in Figure 3b. It is found that this curve is also very similar to that as

Boundaries (labeled in Figure 1)	Flow	Particles
Inflow	Water volume flow rate: 0.426 $m^3\,min^{-1}$	Experiment 1 (a)mass injection rate: $5.81 \cdot 10^{-2}\,kg\,s^{-1}$; (b) particle diameter: 3.5 mm. Experiment 2 (a) mass injection rate: $5.81 \cdot 10^{-5}\,kg\,s^{-1}$; (b) particles are divided into 10 groups with diameter of: 74, 129, 173, 213, 250, 288, 330, 380, 444, 536 μm. Each group has equal mass fraction, i.e., 10 wt%.
Outflow	Pressure outlet	Particle escaping
Top water surface	Free slip (no shear)	Particle capturing
Walls	No slip wall	Particle/wall interaction, see Equation 26

Table 6. Boundary conditions for the calculation of flow and particle motion. The mass flow rate for the experiment 2 with particle diameter (50–600 μm) is reduced by a factor of 0.001, so that the number of particles can be manageable by the current computer facility.

Model parameters	Settings
Turbulence model parameters	$Pr_{t,k} = 1$, $Pr_{t,\varepsilon} = 1.3$, $C_\mu = 0.09$, $C_{1\varepsilon} = 1.44$, $C_{2\varepsilon} = 1.92$
Wall functions	Standard k–ε wall functions
Pressure-velocity coupling	PISO, Gauss-Green discretization for gradients
Flow time-space discretization	Steady state, 1 st order upwind
Particle trajectory integration	Crank–Nicolson scheme
Particle–wall interaction parameters	$\varepsilon_{wall} = 0.8$, $\mu_{wall} = 0.2$
Water density	$998.2\,kg\,m^{-3}$
Water kinematic viscosity	$1.0048 \cdot 10^{-6}\,m^2\,s^{-1}$
Density of particles (experiment 1)	$950\,kg\,m^{-3}$
Density of particles (experiment 2)	930 (averaged) $kg\,m^{-3}$

Table 7. Settings of the numerical model and physical properties of materials.

calculated and measured by Odenthal.[11] No detailed analysis of the global flow pattern in this tundish is presented here. Interested readers can refer to ref.[11] One more statement is that the current numerical model for the flow, defined by Equation 1–7, was already verified against ref.[11]

4. Results and Discussion

The calculation of particle motion is based on the velocity field of Figure 3. Sequences of the particle distribution after particle injection for two experiments are shown in **Figure 4** and **5**, correspondingly. Due to the transparency of the water, particles as observed by the speed camera represent all particles in the tundish in the recording direction. Therefore, the simulation results are post-processed and the particles as seen in Figure 4 and 5 represent all particles in the tundish volume which are projected onto the symmetry plane.

The particles in the water experiment were entrapped by the wooden frame being immersed by 50 mm under the free surface level, restricting the transversal motion of the particles after their flotation. This condition gives an advantage for the comparison with a numerical simulation, since a special separation criterion[10] becomes

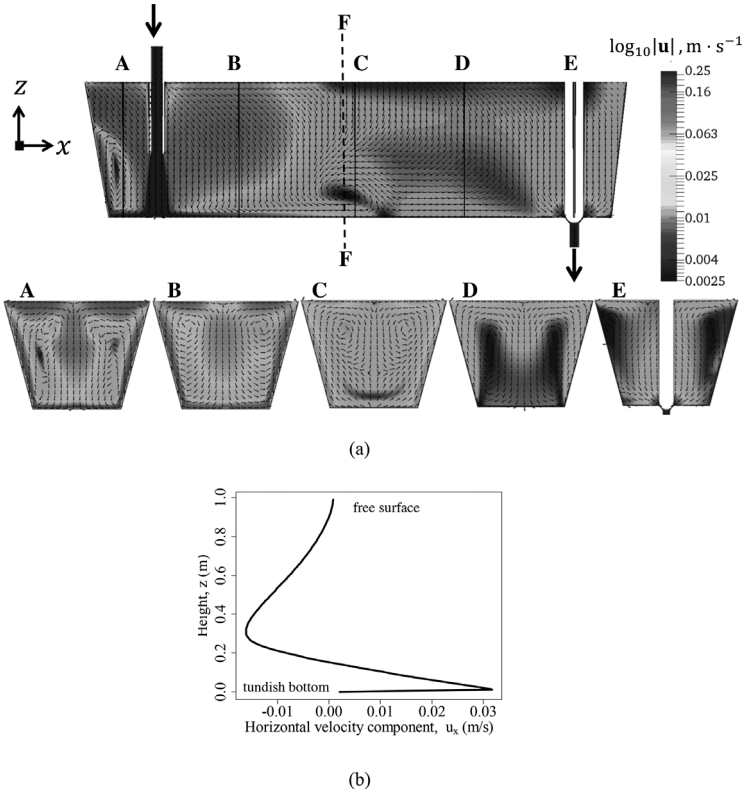

Figure 3. Calculated flow pattern in the tundish: a) velocity field at the mid plane and at some vertical cross-sections (vectors show the flow direction in the cut-planes); b) x-component of the velocity along the vertical line F–F, which crosses through the vortex center.

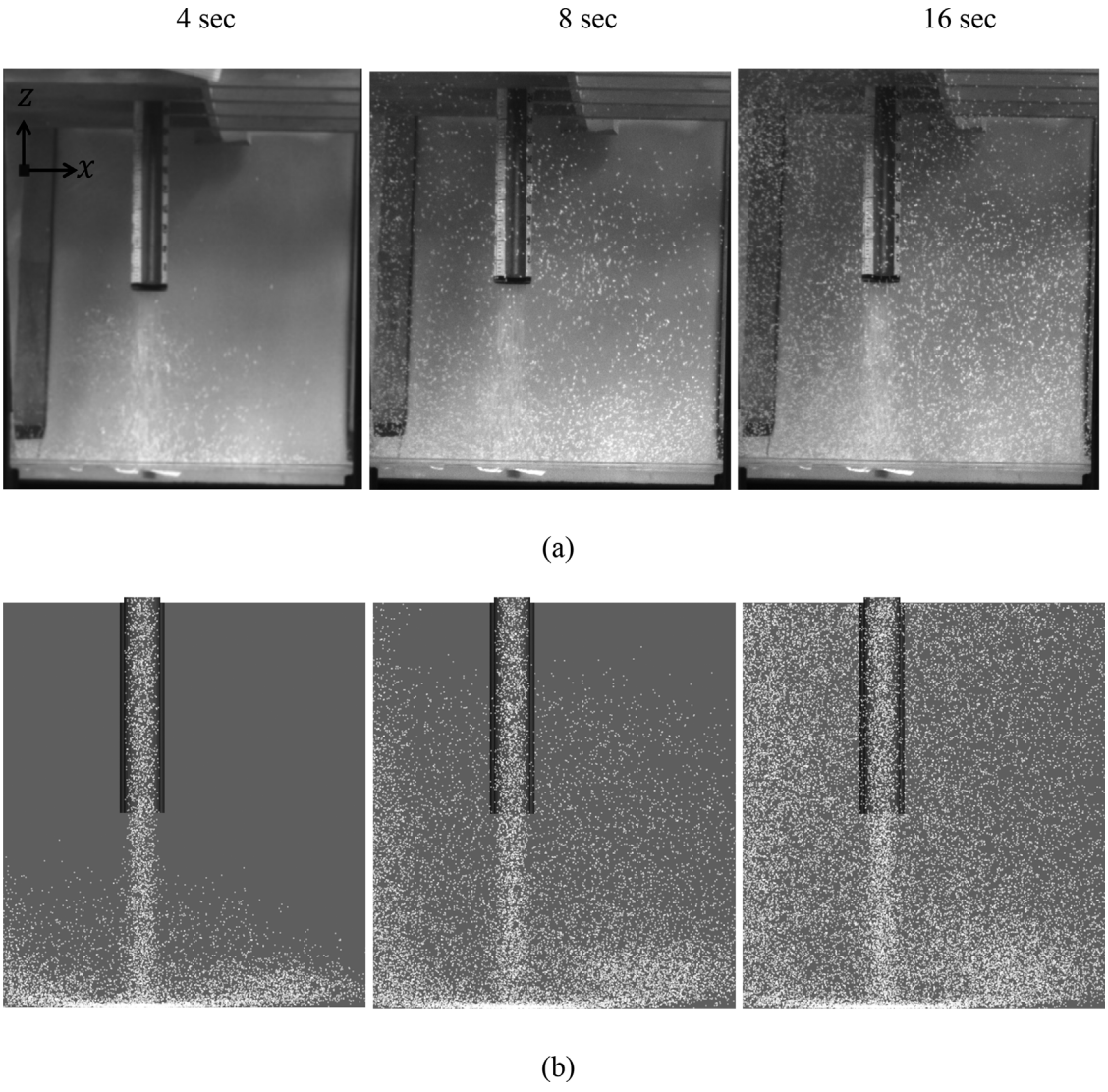

Figure 4. Comparison of particle distribution between the experiment a) and the simulation b) for the case of experiment 1 with particle diameter of 3.5 mm.

unnecessary. Due to the fact that there is only a slight density difference between the particles and the fluid (see Table 3 and 7), the influence of the buoyancy force is diminished, and all other particle–fluid interaction forces described early come into play. This allows performing extensive numerical studies based on the presented experimental data set.

By comparison between simulations and experiments, it is found that a very good simulation–experiment agreement is obtained for the experiment 1 with large diameter of particles (3.5 mm), Figure 4. For the experiment 2 with small diameter of particles (50–600 μm), however, relative large mismatch is obtained, Figure 5. The dissipation of particles seems to be underestimated by the simulation. History of the mass balance of the injected particles is shown in **Figure 6**. They include the total mass of particles as injected into the tundish, the mass of particles as remained in the tundish, the mass of particles as captured by the wooden frame, and the mass of particles as escaped through the outflow. As no such history can be measured experimentally, the simulation result is presented here as reference for interested readers who might compare their modeling results with the current one. One experimentally approved fact can be confirmed by the numerical simulation: for the experiment 1 with large diameter of particles, all particles are finally observed experimentally and predicted numerically to be floated onto the top surface, and no particle escaped from the outflow. The time for the first particle to reach the top water surface and be captured by the wooden frame is predicted ca. 6 s, which agrees to the experiment ideally. For the experiment 2 with the small diameter of particles,

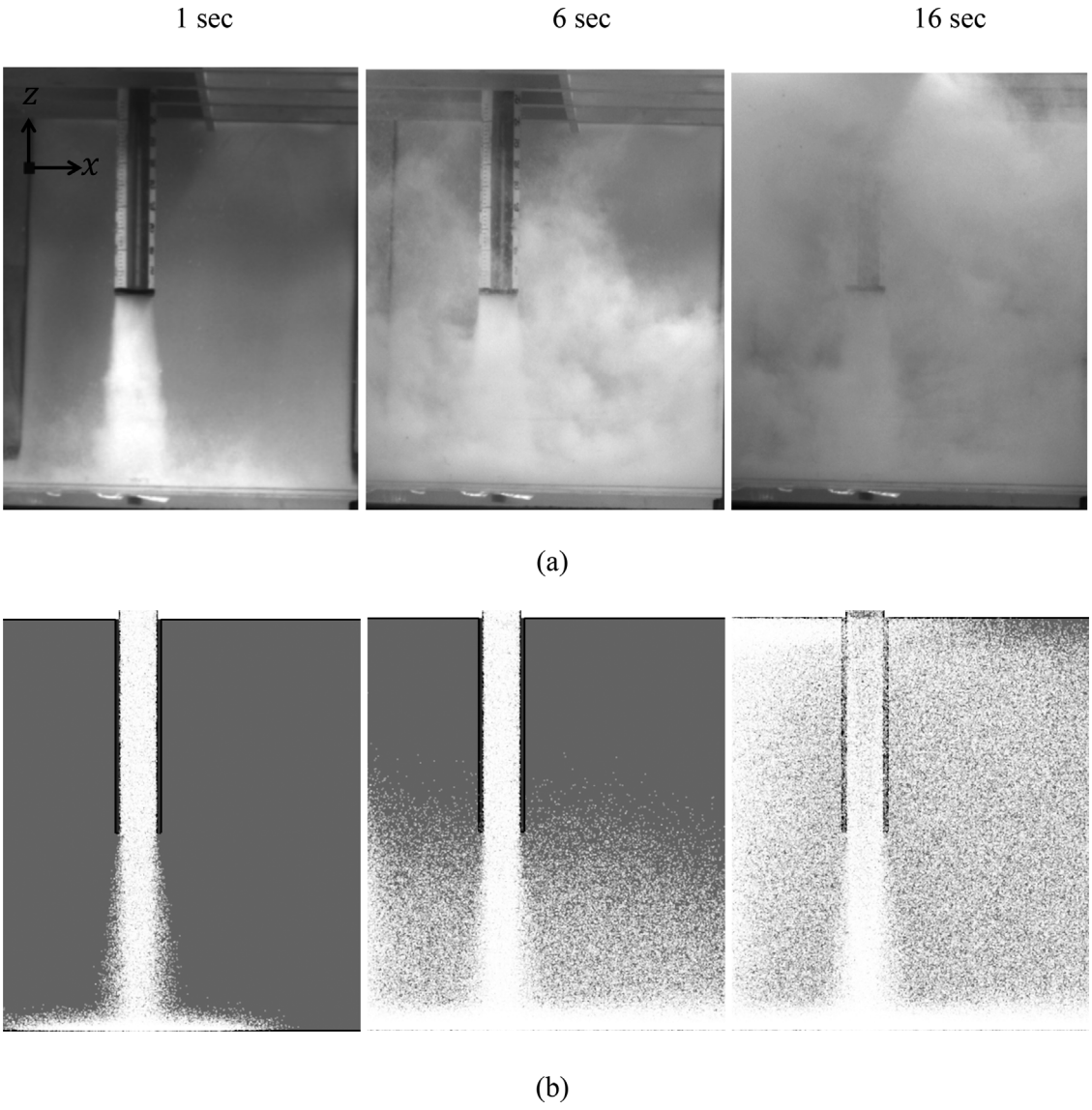

Figure 5. Comparison of particle distribution between the experiment a) and the simulation b) for the case of experiment 2 with particle diameter distribution between 50 and 600 μm. Experimentally it is not possible to separate the particles from each other. For the purpose of post-processing of the simulation result, all particles of different size classes can only be shown by the same size of graphic point (2 pixels for each particle).

the simulation–experiment agreement is not satisfied: ca. 9% of injected particles are predicted to escape from the outflow, while ca. 24% of particles are observed to escape from the outflow experimentally. The time for the first particle to reach the top water surface and be captured by the wooden frame is predicted delayed in comparison with the experiment.

The statistical analyses of the particle capture by the wooden frame are summarized in **Table 8** and **9**. The mass fraction of particles, as captured by each individual cell of the wooden frame, is used to analyze the distribution of the finally captured particles by the top surface. The mass fraction is defined by the mass integral of particles as captured by one cell of the wooden frame divided by total mass of particles as captured by first 15 cells (5×3), corresponding to the experimental measurements in Table 3, of the wooden frame in the case of 3.5 mm particles and by first 20 cells (5×4) in the case of particles with the diameter variation 50–600 μm, as the particle propagation extend more toward the outflow, than in the experiment 1. By comparison between the simulation and the experiment, excellent agreement for the experiment 1 with large particle is obtained, and bad agreement for the experiment 2 with small particle is obtained. It can be concluded that the current model and modeling parameters seem quite valid for calculation of

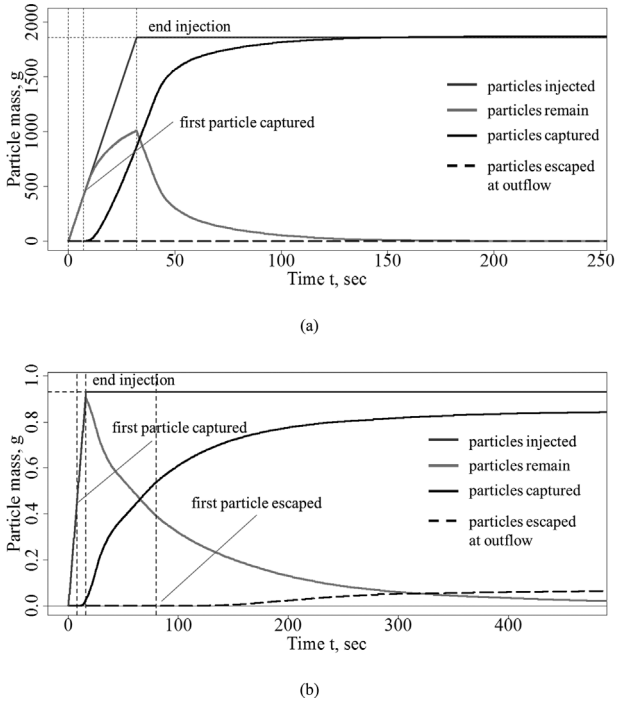

Figure 6. History of the mass balance of the injected particles: mass of particles as remained in the tundish, mass of particles as captured by the wooden frame, and mass of particles as escaped through the outflow. (a) Experiment 1 with particle diameter of 3.5 mm. (b) Experiment 2 with particle diameter distribution between 50 and 600 μm.

the motion of large particle, but not valid for calculation of small particles.

Two main possible reasons for the simulation–experiment mismatch, not requiring deep and extensive studies, are the validity of the one-way coupling approach and the level of the turbulence dissipation of the particles based on the DRW model.

Thereby, the simulation results were first checked for the validity of the one-way coupling approach used in the current study. According to Lain and Garcia,[25] a

Exp./Sim. [wt%]	A	B	C
R1	6.39/9.52	3.17/5.34	0.68/0.2
R2	16.4/15.82	10.32/6.27	1.52/0.29
R3	18.03/15.69	6.56/9.26	0.42/2.06
R4	15.90/14.91	9.22/6.22	1.56/0.28
R5	6.85/8.32	2.33/5.59	0.65/0.22

Table 8. Mass fraction distribution of captured particles for experiment 1 (3.5 mm); comparison between experiment and simulation.

so-called coupling parameter L is defined as a criterion to validate the one-way coupling approach. When $L \ll 1$, the one-way approach is valid. The coupling parameter L is calculated for each volume element as

$$L = \frac{\mathrm{LR}}{1 + \mathrm{St}} \tag{27}$$

where LR is the loading ratio of the flow (the mass ratio between particles and the fluid):

$$\mathrm{LR} = \frac{\rho_\mathrm{p} f_\mathrm{p}}{\rho\left(1 - f_\mathrm{p}\right)} \tag{28}$$

The particle Stokes number St is calculated as follows:

$$\mathrm{St} = \frac{\bar{\tau}_\mathrm{P}}{T_\mathrm{L}} \tag{29}$$

where the relaxation time τ_P of a single particle (see Equation 22) is averaged as $\bar{\tau}_\mathrm{P} = \frac{1}{N} \sum_{i=1\sim N} \tau_\mathrm{p}^i$ for N particles located in a control volume; the integral time scale of turbulence T_L[25] is

$$T_\mathrm{L} = 0.16 \frac{k}{\varepsilon} \tag{30}$$

To check the validity of the one-way coupling the Equation 27 through 30 were used to calculate the coupling parameters in each finite volume. As one can see from Equation 27, the LR parameter is dominant for the estimation of the coupling criterion L especially at the low Stokes numbers. Thereby, the dependency of the coupling factor L against the flow loading ratio LR is shown in **Figure 7** for the big particles simulation. Since the injection is done with the same mass flow rate but for the longer time than in the experiment 2 (see Table 2), a higher particle concentration is expected. Different time instants are analyzed and two the most representative are shown in Figure 7: at the end of injection (32 s), when the highest concentration of particles is detected, and 2 s later. As both plots show, the coupling parameter fulfills the condition $L \ll 1$, approving the one-way coupling approach. Moreover, at the moment of 2 s after the end of injection LR and L parameters decrease to half of the previous values and the one-way coupling criterion remains to be satisfied in the whole simulation domain till the end of the simulation.

The second possible reason for the deviation between the simulation and experimental results could be due to the overestimation of the particle ascending velocity in the DRW model. An isotropic turbulence assumption is made by applying a standard RANS model, allowing the turbulent structures to move in the normal direction to

Exp./Sim. [wt%]	A	B	C	D
R1	6.29/13.1	5.12/6.19	1.12/4.69	1.32/3.19
R2	12.18/8.33	8.97/5.38	4.33/2.81	1.67/1.75
R3	10.69/5.66	6.63/2.81	2.75/1.57	1.91/1.0
R4	11.28/7.34	7.52/4.9	3.69/2.96	1.34/1.67
R5	4.22/12.79	7.97/5.98	0.21/4.77	0.79/3.12

Table 9. Mass fraction distribution of captured particles for experiment 2 (all groups of diameter); comparison between experiment and simulation.

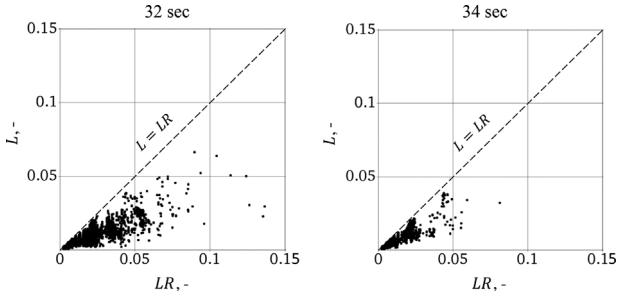

Figure 7. Coupling parameter L (see Equation 27) against the loading ratio LR (see Equation 28) for the case of big particles: each point represents a volume element; parameters are calculated for two time instants of 32 s (end of the injection) and 34 s (2 s after the end of injection).

the free surface. According to the Equation 24, an additional random velocity component is introduced, which can have a dominant effect on the particle acceleration toward the water free surface. In **Figure 8** the ratio distribution between the maximum stochastic component $\mathbf{u}'$ and the mean flow velocity $\mathbf{u}$ is shown. As one can observe in Figure 8, there are well defined areas in the horizontal cut-plane close to the free surface (10 mm below it), where the given ratio is bigger than 1 (dark red color), meaning that the turbulent component $\mathbf{u}'$ dominates the mean velocity. They are mostly located close to the centerline and in the corners of the tundish, partially explaining the mismatch between the

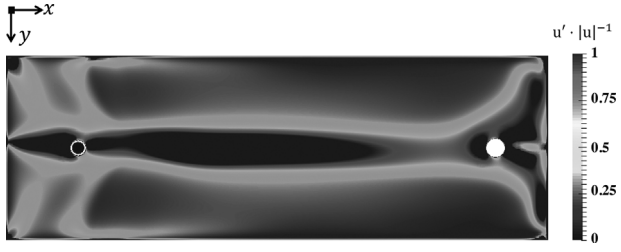

Figure 8. Distribution of the ratio between the maximum $\mathbf{u}' = \sqrt{\frac{2k}{3}}$ and the mean velocity $\mathbf{u}$ on the plane 10 mm bellow the water free surface.

experimental data and the simulation results in those areas. However, the total exclusion of the particle–eddy interaction from the numerical model leads to unphysical results.

Other possible reasons for the simulation–experiment disagreement for the experiment 2 are as follows: (i) the simplification of the particle size distribution; (ii) the improper assumption of quasi-steady state flow; (iii) the ignorance of the particle–particle interaction, e.g., particle agglomeration; and (iv) exclusion of the mounted wooden frame from the simulation, etc. Discussion on these issues requires further deep studies and is out of the scope of this publication.

5. Conclusion

A water experiment benchmark of a continuous casting tundish at the engineering scale is presented. During the water flow experiment plastic particles with the density slightly smaller than water density are injected into the model tundish, and then their motion is recorded by high-speed camera. Additionally, the particles which float-up to the water surface in the tundish are captured by an instrumented wooden frame and their weight is recorded after all. The goal of the publication is to call contributions from researchers to propose new models or improve the existing models by validating them against the same experiment. In the second part of this paper, an Eulerian–Lagrangian model is used to calculate the benchmark cases. It is found that for the water experiment with large particles (diameter of 3.5 mm), the numerical simulation results agree quantitatively with the experiment. For the experiment with small particles (diameter of 50∼600 μm), however, the quantitative mismatch between the simulation and the experiment is quite large. It means that the existing model, widely used both in the commercial and the open-source CFD code, can only be used to predict the motion of particles qualitatively, and it is still subject to further improvements before it is used for quantitative simulation of industry processes.

Acknowledgements

The authors acknowledge financial support from the Austrian Federal Ministry of Economy, Family, and Youth and the National Foundation for Research, Technology, and Development within the framework of the Christian Doppler Laboratory for Advanced Process Simulation of Solidification and Melting.

Received: July 27, 2016; Revised: August 26, 2016

Keywords: continuous casting; tundish; non-metallic inclusion; Eulerian–Lagrangian; turbulent flow

Nomenclature

DRW	discreet random walk model
NMIs	non-metallic inclusions
RANS	Reynolds-averaged Navier–Stokes equations
C_μ, $C_{1\varepsilon}$, $C_{2\varepsilon}$	turbulence model constants
D_P	particle diameter
$\mathbf{F}_B$	buoyancy force
$\mathbf{F}_D$	drag force
$\mathbf{F}_L$	lift force
$\mathbf{F}_P$	pressure gradient force
$\mathbf{F}_V$	virtual (added) mass force
G	shear production of turbulence kinetic energy
L	coupling parameter
LR	loading ratio of the flow
L_{eddy}	eddy length scale
$Pr_{t,k}$	turbulent Prandtl number for turbulent kinetic energy
$Pr_{t,\varepsilon}$	turbulent Prandtl number for turbulent kinetic energy
Re_P	particle Reynolds number
Re_G	particle shear Reynolds number
T_L	integral time scale of turbulence
f_P	particle volume fraction
$\mathbf{g}$	gravity
k	turbulent kinetic energy
m_P	particle mass
p	pressure
r	uniform random number
t	time
t_{cross}	eddy crossing time
t_{eddy}	characteristic eddy life time
t_P^{DRW}	action time of current DRW parameters
$\mathbf{u}$	mean velocity
$\mathbf{u}'$	stochastic part of mean velocity
$\mathbf{u}_P$	particle velocity
$\mathbf{u}_P^n$	particle velocity normal component
$\mathbf{u}_P^\tau$	particle velocity tangential component
$\mathbf{x}_P$	particle trajectory vector
$\dot{\gamma}$	shear rate in fluid
$\dot{\boldsymbol{\varepsilon}}$	rate-of-strain tensor
ε	turbulence dissipation rate
ε_{wall}	wall restitution factor
μ_{eff}	effective viscosity
μ_ℓ	molecular dynamic viscosity
μ_t	turbulent dynamic viscosity
μ_{wall}	wall friction coefficient
$\boldsymbol{\zeta}$	normal random number
ρ	density
ρ_P	particle density
τ_P	particle relaxation time

References

[1] R. I. L. Guthrie, *Metall. Mater. Trans. B* **2004**, *35B*, 417.
[2] L. Zhang, B. G. Thomas, *ISIJ Int.* **2003**, *43*, 271.
[3] K. Schwerdtfeger, *Archive für Eisenhüttenwesen*. **1983**, *54*, 87.
[4] H. J. Odenthal, H. Pfeifer, M. Klaas, *Steel Res. Int.* **2000**, *71*, 210.
[5] B. G. Thomas, Q. Yuan, S. Mahmood, R. Liu, R. Chaudhary, *Metall. Mater. Trans. B* **2014**, *45B*, 22.
[6] C. Pfeiler, M. Wu, A. Ludwig, *Mater. Sci. Eng. A* **2005**, *413*, 115.
[7] M. Javurek, B. Kaufmann, *PAMM Proc. Appl. Math. Mech.* **2003**, *3*, 406.
[8] L. P. Wang, C. Peng, Z. Guo, Z. Yu, *Comput. Fluids* **2016**, *124*, 226.
[9] R. R. Zhu, W. B. Zhu, L. C. Xing, Q. Q. Sun, *Powder Technol.* **2011**, *210*, 73.
[10] A. Rückert, M. Warzecha, R. Koitzsch, M. Pawlik, H. Pfeifer, *Steel Res. Int.* **2009**, *80*, 568.
[11] H. J. Odenthal, M. Javurek, M. Kirschen, *Steel Res. Int.* **2009**, *80*, 264.
[12] A. Vakhrushev, A. Ludwig, M. Wu, Y. Tang, G. Nitzl, G. Hackl, *Proc. of 4th Int. Conf. Simulation and Modeling in Metallurgical Processes in Steelmaking (STEELSIM 2011)*, SREELSIM 2011 CD-Rom Proceedings, Düsseldorf **2011**, *S17*, 1.
[13] H. G. Weller, G. Tabor, H. Jasak, C. Fureby, *Comput. Phys.* **1998**, *12*, 620.
[14] C. M. Rhie, W. L. Chow, *Proc. of 3rd Joint Thermophysics, Fluids, Plasma and Heat Transfer Conf.*, St. Louis **1982**.
[15] J. H. Ferziger, M. Perić, in *Computational Methods for Fluid Dynamics*, 3rd Ed., Springer-Verlag, Berlin, Heidelberg **2002**, Ch. 7.2.
[16] W. P. Jones, B. E. Launder, *Int. J. Heat Mass Trans.* **1973**, *15*, 301.
[17] B. E. Launder, B. I. Sharma, *Lett. Heat Mass Trans.* **1974**, *1*, 131.
[18] B. E. Launder, D. B. Spalding, in *Lectures in Mathematical Models of Turbulence*, Wiley-VCH Verlag **1972**.

[19] L. Schiller, Z. Naumann, *Z. Ver. Dtsch. Ing.* **1933**, *77*, 318.
[20] C. T. Crowe, J. D. Schwarzkopf, M. Sommerfeld, Y. Tsuji, in *Multiphase Flows with Droplets and Particles*, 2nd Ed., CRC Press, Boca Raton, London, New York, Washington, D.C. **2011**, Ch. 4.
[21] P. G. Saffman, *J. Fluid Mech.* **1965**, *22*, 385.
[22] Q. Wang, K. D. Squires, M. Chen, J. B. McLaughlin, *Int. J. Multiphase Flow* **1997**, *23*, 749.
[23] D. I. Graham, P. W. James, *Int. J. Multiphase Flow* **1996**, *22*, 157.
[24] D. I. Graham, *Int. J. Multiphase Flow* **1996**, *22*, 177.
[25] S. Lain, J. A. Garcia, *Chem. Eng. Sci.* **2006**, *61*, 6775.